Mon. Not. R. Astron. Soc. **000**, 1–17 (2020) Printed 26 December 2020 (MN LATEX style file v2.2)

Measurement of turbulence profile from defocused ring images

A. Tokovinin⋆
Cerro Tololo Inter-American Observatory / NSFs' NOIRlab, Casilla 603, La Serena, Chile

-

ABSTRACT
A defocused image of a bright single star in a small telescope contains rich information on the optical turbulence, i.e. the seeing. The concept of a novel turbulence monitor based on recording sequences of ring-like intrafocal images and their analysis is presented. It can be implemented using standard inexpensive telescopes and cameras. Statistics of intensity fluctuations in the rings and their radial motion allow measurement of the low-resolution turbulence profile, the total seeing, and the atmospheric time constant. The algorithm of processing the images and extracting the turbulence parameters is developed and extensively tested by numerical simulation. Prescriptions to correct for finite exposure time and partially saturated scintillation are given. A prototype instrument with a 0.13-m aperture was tested on the sky. The RINGSS (Ring-Image Next Generation Scintillation Sensor) can be used as a portable turbulence monitor for site testing and as an upgrade of existing seeing monitors.

Key words: site testing – atmospheric effects

1 INTRODUCTION

A live image of a bright star in a small slightly defocused telescope displays distortions caused by the optical turbulence, "seeing". Movies of such images captured by a fast camera can be interpreted to measure turbulence strength, its distribution along the line of sight, and the characteristic time scale. Extraction of quantitative information on turbulence from the fast movies of ring-like defocused images is the subject of this paper. A turbulence monitor based on this idea consists of a small telescope and a fast camera; its hardware is standard and inexpensive, while the major challenge lies in the software needed to process the movies.

Measurement of the vertical distribution of optical turbulence in the terrestrial atmosphere (OTP – optical turbulence profile) serves to support operation of modern astronomical observatories equipped with adaptive optics (AO) instruments and to characterize new astronomical sites. A classical instrument to measure the OTP using scintillation of double stars, SCIDAR, needs aperture sizes on the order of 1 m and therefore it is not suitable for testing remote sites (e.g. Klueckers et al. 1998). A Multi-Aperture Scintillation Sensor (MASS) delivers low-resolution OTPs using scintillation of bright single stars and a small aperture of $\sim$0.1 m (Kornilov et al. 2003). Combination of MASS with the Differential Image Motion Monitor (DIMM, Sarazin & Roddier 1990) in one instrument attached to a small telescope has become a standard tool for site testing and monitoring (Kornilov et al. 2007). About 35 such instruments have been fabricated and used in the site characterization projects (e.g. Schöck et al. 2009) and for turbulence monitoring at existing observatories.

MASS records scintillation signals from four concentric annular apertures using photo-multipliers. This technology became obsolete when fast low-noise panoramic detectors, such as electron-multiplication (EM) CCDs and scientific CMOS, became available. Moreover, the opto-mechanics and electronics of the MASS-DIMM instruments are custom-made and difficult to replicate. Nowadays, MASS-DIMM should be replaced by an instrument based on solid-state light detectors.

The need to find an alternative to MASS has been generally recognized. In a master thesis project, Kohlman (2018) constructed a prototype where the flux in four concentric annuli within a 15-cm unobstructed aperture was measured by a CMOS camera, emulating MASS. An alternative approach is adopted by the team at the Pontificia Catolica University in Chile (Guesalaga et al. 2016); they also record intensity fluctuations at the pupil, but interpret them differently by taking a one-dimensional Fourier transform in the angular coordinate of nar-

⋆ E-mail: atokovinin@ctio.noao.edu

row rings carved from the pupil images. This approach circumvents the problem of centrally obstructed apertures of standard small Schmidt-Cassegrain telescopes. The instrument is called FASS (Full-Aperture Scintillation Sensor), and its development continues (Guesalaga et al. 2020).

Recording scintillation signals at the telescope pupil with a solid-state detector requires a large optical de-magnification factor $k_{\rm magn} \sim 10^3$ to match the small physical size of pixels and the spatial scale of scintillation. The latter is set by the Fresnel radius $\sqrt{\lambda z} = 1.7$ cm for a propagation distance of $z = 0.5$ km and a wavelength of $\lambda = 0.6\,\mu$m. If the detector pixels projected on the pupil are much smaller than the Fresnel radius, the number of photons per pixel received from even bright stars in a short 1-ms exposure time would be small compared to the detector readout noise. The EM CCDs have a readout noise of less than one electron (el) and allow noiseless on-chip binning, thus alleviating the de-magnification challenge; this option was used in FASS (Guesalaga et al. 2016). However, noiseless binning is not possible in CMOS cameras, while their readout noise is about 1 el. Hence, a large $k_{\rm magn}$ is indeed necessary with a CMOS. Maximum optical de-magnification is limited by the Lagrange invariant (the product of surface and solid angle is constant). Even with a large solid angle at the detector, the maximum angle on the sky (i.e. the field of view) is on the order of an arcminute. Therefore, a solid-state scintillation sensor requires an additional guiding camera to keep the star centred in the narrow field.

Combination of MASS and DIMM in one instrument solves the guiding problem (which is done by DIMM), at the cost of having two parallel systems with separate detectors, acquisition channels, and software. DIMM measures the total seeing including the ground layer, to which MASS is insensitive. This combination is a consequence of the physics of optical propagation. Phase distortions of optical waves produced by atmospheric fluctuations of the air refractive index are partially converted into amplitude fluctuations (scintillation) only after propagation. Therefore, any scintillation-based instrument is intrinsically insensitive to turbulence near the ground, and only instruments sensitive to phase distortions (like DIMM) can measure the total seeing.

In reality, this distinction between a phase-sensitive DIMM and an amplitude-sensitive MASS is blurred because DIMM is also affected by amplitude fluctuations to some extent and its measurements depend on the propagation distance (Tokovinin & Kornilov 2007; Kornilov & Safonov 2019). On the other hand, by measuring scintillation in a plane optically conjugated below the pupil, a virtual propagation path is added, making a scintillation-based instrument sensitive to the near-ground turbulence. This is the principle of a generalized SCIDAR (Klueckers et al. 1998; Osborn et al. 2018). Strictly speaking, virtual propagation works for an aperture of infinite size because diffraction on its edges intervenes at a spatial scale of the order of $\sqrt{\lambda H}$ for a virtual propagation distance H. This is not a problem in a SCIDAR because in a large-aperture telescope the area near the edges affected by diffraction is relatively small. However, in a small telescope the diffraction affects the whole aperture and must be taken into account explicitly if virtual propagation is used. Moreover, a defocused pupil image is affected by the telescope shake, aberrations, and low-altitude (local) turbulence, whereas a pupil-based scintillation sensor is immune to all these effects.

Extending the scintillation-based technique to measure the full seeing is an attractive choice that allows to get rid of the DIMM. This option is currently explored by the FASS team (Guesalaga et al. 2020). The pupil image conjugated to some distance H below the ground is obtained simply by defocusing the telescope. When the detector is placed at a distance Δ in front of the focal plane, it is conjugated to $H = F^2/\Delta$, where F is the telescope focal distance. By using a moderate-sized telescope of $D = 30$ cm diameter and conjugating to H of a few hundred metres, it is possible to select an annular zone in the defocused image that is not strongly distorted by diffraction and thus is suitable for Fourier analysis of intensity fluctuations in the angular coordinate, as in the aperture-conjugated FASS.

On the other hand, when the two apertures with prisms that produce two images in a classical DIMM are replaced by a weak conic lens (axicon), a ring-like image is formed at the focal plane. Such extension of DIMM to the full aperture increases its sensitivity and eliminates the intrinsic asymmetry of a two-aperture DIMM. The radius of the ring is a measure of the defocus, and its fluctuations caused by turbulence are directly linked to the seeing. Moreover, the speed of defocus variation allows us to measure the atmospheric time constant – an important parameter that affects AO systems and interferometers. A turbulence monitor based on ring images was called FADE (FAst DEfocus) and tested using a 35-cm telescope (Tokovinin et al. 2008).

The proposed concept is a fusion of previous ideas. It is based on fast registration of ring-like images, as in FADE. Fluctuations of intensity along the ring (in the angular coordinate) reflect intensity variation in the annular aperture and are analogous in this sense to FASS. On the other hand, the ring is focused in the radial direction, and radial motion of its segments gives a measure of the total seeing, as in DIMM. A descriptive acronym RINGSS (Ring-Image Next Generation Scintillation Sensor) is chosen for this concept to underline its descendence from MASS and FASS.

Propagation of optical waves through turbulent atmosphere is a complex phenomenon. Moreover, the standard description of turbulence refers to its idealized statistical model. As a result, turbulence parameters cannot be defined or measured with arbitrary accuracy, and all instruments measuring optical turbulence are based on approximations. This point, further elaborated in Tokovinin & Kornilov (2007), is important to bear in mind. That paper, among many others, lists the definitions of standard turbulence parameters – the seeing ϵ_0, the Fried radius $r_0 = 0.98\lambda/\epsilon_0$, the refractive-index structure constant C_n^2, etc.

The operational principle of RINGSS is presented in Section 2. Its main component – the algorithm to measure turbulence parameters from ring images – is exposed in Sections 3 to 5. On-sky tests of a prototype instrument are covered in Section 6 and the choice of instrument parameters in Section 7. Discussion of this new method in Section 8 closes the paper.

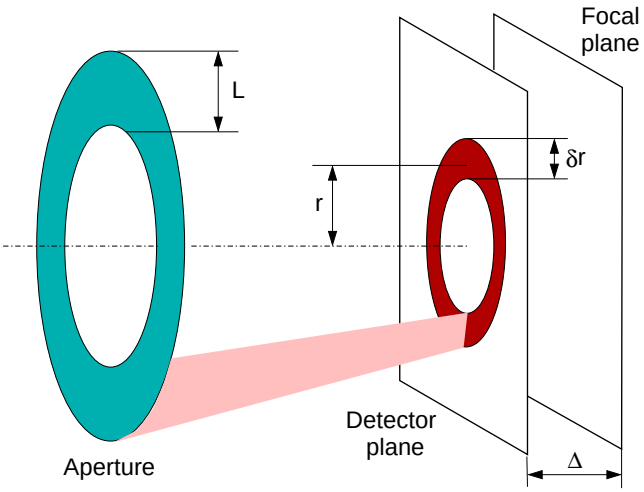

Figure 1. Principle of the ring-image turbulence monitor. Light from a single bright star is collected by a telescope with an annular aperture and some conic aberration. The image is a ring with angular radius r and angular width of $\delta r = \lambda/L$ set by diffraction, where $L = D(1-\epsilon)/2$ is the width of the aperture annulus. Fluctuations of intensity along the ring are mostly produced by amplitude fluctuations at the aperture (scintillation), while deformation of the ring is caused mostly by phase aberrations. Statistics of these fluctuations enable measurement of the turbulence profile and seeing.

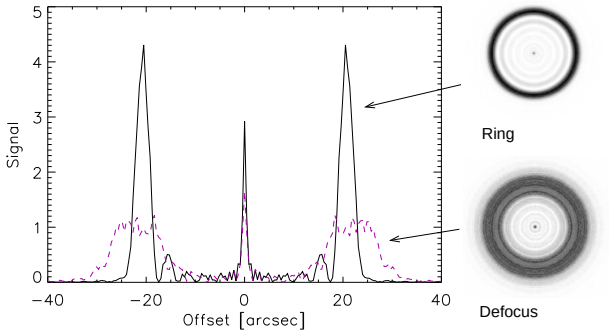

Figure 2. Comparison between the focused ring produced by a conic wavefront and an equivalent defocused image. The curves show cuts through the images ($D = 0.13$ m, $\epsilon = 0.5$, $H = 0.4$ km).

2 OPERATIONAL PRINCIPLE OF RINGSS

The method of signal analysis developed here is applicable to three kinds of data: (i) images of annular telescope pupil, (ii) simple defocused images, and (iii) defocused images sharpened in the radial direction. The last option appears to be the best choice and is considered here, while the pupil-plane case (i) is analogous to FASS. The geometry and basic parameters are introduced in Fig. 1. An annular aperture of diameter D with a central obscuration ϵ has a width of $L = D(1-\epsilon)/2$. The angular width of a focused ring image is set by diffraction to $\delta r \approx \lambda/L$ (at $\epsilon > 0.5$). The ring angular radius is $r_{\rm ring,rad} \approx D(1+\epsilon)/(4H)$, where $H = F^2/\Delta$ is the conjugation distance of the detector ($H = \infty$ at the focal plane) and F is the efective focal length. By selecting a larger defocus Δ, we get a smaller H and a larger ring, with less photons per pixel.

A defocused image in a small telescope with annular aperture is heavily affected by diffraction and, therefore, is a poor representation of the pupil image. When the wavefront is conic, rather than spherical, the ring is focused in the radial direction and becomes sharper. Figure 2 compares these situations. The maximum signal in the radially focused ring is $\sim$3$\times$ larger than in the similarly defocused image. Only when the aperture is a narrow annulus (i.e. with a large ϵ), the distinction between conic and spherical wavefronts within the aperture becomes negligibly small. A practical way to obtain a nearly conic wavefront is to combine defocus with a small spherical aberration of opposite sign. The spherical aberration compensates the curvature of the defocused wavefront within annular aperture and renders it almost conical. As shown by Tokovinin et al. (2008), an excellent approximation is achieved when the ratio of rms spherical to rms defocus aberrations is 1:10. Such condition can occur when a positive lens is used as a focal reducer.

The linear size of the detector pixel p and the need to collect enough photons per pixel favor a short effective focal length F. A defocused image approximates the pupil with a demagnification factor $k_{\rm magn} \approx H/F$. Hence, for a given H, a small F is needed to get a large $k_{\rm magn}$. This can be achieved by a focal reducer – an achromatic positive lens placed in front of the detector. The lens also produces spherical aberration of correct sign to make a conic wavefront. On the other hand, the need to sample the ring in the radial direction by at least two pixels restricts the minimum focal length to $F/D > (p/\lambda)(1-\epsilon)$, or $F/D > 2.4$ for $p = 2.9$ μm, $\lambda = 0.6$ μm, and $\epsilon = 0.5$.

The RINGSS concept is generic and independent of the instrument parameters chosen to illustrate it. Most numerical examples in this paper refer to a telescope of 0.13 m diameter with $\epsilon = 0.5$ and a detector conjugated to $H = 400$ m, resembling the actual prototype described below. Optimum sampling of the $r_{\rm ring} \approx 25''$ radius ring at $\lambda = 0.6$ μm calls for the relatively coarse pixels of $1.9''$, hence a radius of $\sim$13 pixels.

A ring image is used to compute several *signals* a_m as sums of the products of the pixel values I_i and the *masks* $M_{m,i}$, normalized by the total flux I_0:

$$a_m = I_0^{-1} \sum_i M_{m,i} I_i. \qquad (1)$$

This formulation is very general. It applies to a DIMM instrument where the signals a are spot centroids and the masks are defined accordingly. A Fourier transform of the image can also be viewed as a particular case of (1) where M is a complex exponent and the signals a also are complex numbers.

Use of the Fourier transform for statistical analysis of random intensity distributions appears to be a natural choice. However, the scintillation pattern in a small telescope is truncated by its aperture, and the spatial power spectrum of the intensity distribution at the pupil is a heavily aliased version of the intrinsic power spectrum of the infinite scintillation pattern. Fourier anal-

ysis of scintillation in an annular aperture avoids aliasing when polar coordinates (r, θ) are used. This idea, first implemented in FASS (Guesalaga et al. 2016), is exploited here. The Fourier transform of a ring image in the angular coordinate is a set of complex signals a_m for angular frequencies $m = 0, 1, 2, \ldots$ that correspond to (1) with masks

$$M_m(r, \theta) = f_r(r)\mathrm{e}^{\mathrm{i}m\theta}. \quad (2)$$

Here, $f_r(r)$ is the radial weight needed to reduce the impact of noise in image pixels outside the ring image or pupil. The maximum angular frequency m is set by the Nyquist limit, i.e. at least two pixels along the ring per period. This leads to $m_{\max} = \pi r_{\mathrm{ring}}$, with the ring radius in pixels. A typical value $r_{\mathrm{ring}} = 10$ pixels corresponds to $m_{\max} \approx 30$.

The mean square modulus of the angular signals computed for a series of images is called *angular power spectrum* (APS) S_m, in direct analogy to the standard power spectrum:

$$S_m = \langle |a_m|^2 \rangle = \sum_{j=1}^{N} W_m(z_j) J_j. \quad (3)$$

The right-hand side of (3) relates the APS to the optical turbulence profile (OTP), represented by a collection of N discrete layers at distances z_j from the instrument with turbulence strength $J_j = C_n^2(z_j)\mathrm{d}z$ in each layer. Turbulence integrals J are measured in $\mathrm{m}^{1/3}$; a seeing of $1''$ (at 500 nm wavelength) corresponds to $J = 6.83 \times 10^{-13}\,\mathrm{m}^{1/3}$. The seeing ϵ_0 and the Fried radius r_0 are common turbulence parameters uniquely related to J for a given wavelength (e.g. Tokovinin & Kornilov 2007). An infinite turbulence outer scale is assumed throughout this paper because at the small spatial scales relevant here the outer scale effects are negiligible.

Equation (3) assumes that each turbulent layer gives its independent contribution to the APS, proportional to J_j with a coefficient $W_m(z_j)$ called *weighting function* (WF). This assumption holds in the weak scintillation regime. Modelling the combined effect of turbulence by a linear combination of effects produced by all layers is the cornerstone principle of all turbulence monitors, without exception. In the case of a DIMM, for example, the WFs are often assumed to be independent of z and the DIMM signal is related to the total turbulence integral, i.e. to the seeing.

The APS at $m = 0$ is the normalized variance of the total flux, also called scintillation index. With increasing m, the APS isolates a band of increasing spatial frequencies from the scintillation spectrum. As the characteristic scale of the scintillation is of the order of $\sqrt{\lambda z}$, a small-scale scintillation (i.e. large m) is produced mostly at small z, while a large-scale scintillation corresponds to a large z. A set of WFs plotted in Fig. 3 illustrates their dependence on z and m: S_{10} is mostly sensitive to turbulence within 1 km, while S_1 measures mostly the distant turbulence. Owing to the different z-dependence of the WFs, equation (3) can be inverted, solving for a set of turbulence integrals J_j that match the measured APS S_m. This is the common operational principle of MASS, FASS, and RINGSS. The differences between them are in the input signals and in the WFs.

In addition to measuring the OTP from scintillation,

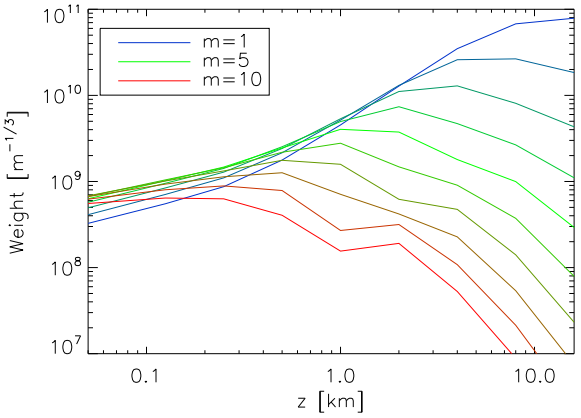

Figure 3. Weighting functions for the APS from $m = 1$ to $m = 10$. Instrument parameters: $D = 0.13$ m, $\epsilon = 0.5$, $H = 400$ m, polychromatic light (a star of effective temperature 7500 K).

RINGSS provides an alternative estimate of the seeing from the differential image motion, as in a DIMM. This extra benefit is not available when the telescope is simply defocused without radial ring sharpening. Radial deformations of the ring are estimated similarly to the angular coefficients, i.e. by summing products of pixel values and masks. The ring is divided into eight 45° sectors and the radius in each sector is computed by the centroid algorithm a with suitable radial mask (eq. 4 below). The rationale for computing radii by sectors is twofold. First, it gives four DIMM-like signals of longitudinal distances between opposite sectors (sum of their radii) for measuring the seeing. Second, it allows to determine the position of the ring centre from the difference between the opposite radii. This provides a robust way to centre the ring in each frame.

Summarizing, the operational principle of RINGSS is similar to that of MASS and FASS. Series of ring images are recorded and processed to extract the angular signals a_m and the sector radii. The variances of these quantities are interpreted in terms of the turbulence profile J_j by solving a system of linear equations with appropriate WFs. The two key components of RINGSS are the algorithms for computing the signals and the calculation of the WFs; they are covered in the following Sections. These algorithms were verified using both simulated and real data.

3 IMAGE PROCESSING

Series of consecutive ring images (image cubes) are processed to determine angular signals (or coefficients) a_m, sector radii r_k, and several additional parameters such as background, ring radius, noise estimates, etc. The image cubes can be recorded on a disk by the acquisition software or passed to the processing pipeline directly without saving, as done typically in a DIMM. Series of signals extracted from the image cubes are then used to

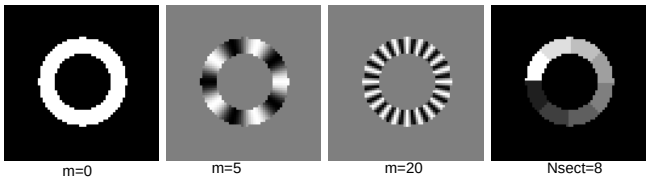

Figure 4. Spatial masks applied to the 64×64 pixels ring images. The first panels show three cosine filters, the last panel is a sum of the sector masks F_k, each multiplied by k to distinguish the sectors.

compute statistical moments (variances and covariances) needed for the OTP measurement.

3.1 Calculation of the signals

Spatial masks have the same size as the image frames, e.g. 64×64 pixels. The masks for computing the real and imaginary (cosine and sine) parts of the angular signals a_m are given by eq. 2. The radial mask $f_r(r)$ equals one for all pixels with radii within the mask half-width Δr from the ring radius $r_{\rm ring}$ (in pixels) and zero otherwise. A smooth (e.g. Gaussian) $f_r(r)$ was tested, but the simple sharp radial cutoff works quite well. The default choice is $\Delta r = 1.5\delta r$, where δr is the full width at half maximum (FWHM) of the ring, i.e. its thickness. Using a smaller mask width decreases the noise, but produces biased results (e.g. under-estimated seeing), as demonstrated by simulations, while a wider mask increases the noise without affecting other parameters. Figure 4 illustrates the cosine masks with $m = 0, 5, 20$.

For measuring the ring radius, we divide it into $N_{\rm sect} = 8$ radial sectors, each sector covering 45° in angle. For a sector k, the mask $F_k = f_r(r)$ within the sector and zero otherwise; it measures the total signal (flux) within the sector. The mask $R_k = rF_k$ estimates the ring radius in this sector:

$$r_k = \sum_i R_{k,i} I_i / \sum_i F_{k,i} I_i. \qquad (4)$$

3.2 Centring the rings

Each frame must be centred and the background must be subtracted before computing the products of pixel values and masks. Also, the ring radius and width must be known to define the masks. The parameters $r_{\rm ring}$ and δr can be fixed for a given instrument, but currently they are estimated 'on the fly' from the average first 50 frames of the image cube, to reduce the noise. The background is also estimated from the average image as the median value of all its pixels outside $1.5r_{\rm ring}$.

Centring of each frame is a critical part of the algorithm. The sector radii computed by (4) give an estimate of the residual ring offsets dx (similarly dy) as

$$dx = (2.3/N_{\rm sect}) \sum_k r_k \cos\theta_k, \qquad (5)$$

where θ_k are the angles of the sector centres, and the proportionality coefficient 2.3 was determined by processing artificially shifted images. The offsets determined from the current frame are applied to centre the following frame, so accurate tracing of the ring motion is achieved. This algorithm was found to be very robust.

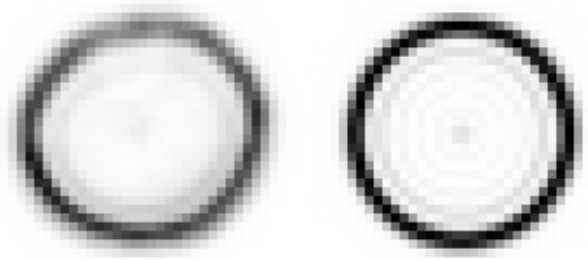

Figure 5. Comparison of the average centred ring image in the prototype instrument (left) and the simulated undistorted image with matched parameters (right).

The frames should be centred within a fraction of a pixel. When the centring is done only within one pixel (by integer image shifts), the estimated centres are biased to integer values, so the curves of displacement vs. frame number computed for simulated image cubes with ring motion are distorted. Moreover, integer shifts introduce a sub-pixel jitter of the otherwise static ring and cause fluctuations of the differential sector radii and the angular signals that exceed the photon-noise errors at high flux. Fractional sub-pixel shifts by bilinear interpolation were tested to fix this issue. However, interpolation introduces correlation between pixels and affects the shape of the noise spectrum, damping it at high frequencies. Finally, sub-pixel shifts by Fourier transform are implemented. Unlike interpolation, they do not distort the noise statistics.

Re-centred frames are summed up (averaged) and saved for off-line examination. Figure 5 compares the average re-centred image from a real instrument with the ideal diffraction image. Note the similarity of the diffraction structure, e.g. the faint inner ring and a small spike at the centre. The real average ring is wider, being affected by distortions under a $2''$ seeing. Its non-uniformity in azimuth is caused by small residual optical aberrations of the telescope, in particular coma and astigmatism.

To compute the radii for $N_{\rm sect} = 8$ sectors and 31 a_m complex signals for $0 < m < m_{\rm max} = 30$, a total $2N_{\rm sect} + 2(m_{\rm max} + 1) = 78$ masks are needed. Calculation of all signals is implemented as a matrix-vector product. Pixel values I_i in a 64×64 frame (after centring and background subtraction) are arranged in a single 4096-element vector, and all masks are combined in a 78×4096 mask matrix. However, with a sharp radial mask, only the pixels inside the mask are used. This reduces the dimension of the mask matrix from 4096 to ∼1000 elements per line and speeds up the calculation. For example, processing a cube of 64×64×2000 format on a laptop takes 1.06 s with the full matrix and only 0.44 s with the reduced matrix.

Processing of the image cube results in a matrix of the signals and returns additional parameters such as the ring radius and width, its average centre (useful for automatic guiding), back-

ground, flux, and the factors ν needed to estimate the noise (see below).

3.3 Noise estimation

Without turbulence, the ring image is static (it only moves as a whole owing to the telescope tracking errors), but the signals still fluctuate because of the photon and readout noise. Comparison between analytic estimates of the noise variance and the variance computed on simulated cubes is a good test of the algorithm. The noise variance (bias) must be subtracted from the measured APS and from the variance of the differential sector motion for correct estimation of the atmospheric parameters.

Let I_i be the pixel values in photo-electrons. Their variance is $I_i + R^2$, where R is the readout noise in electrons, assumed to be equal in all pixels. To estimate the APS of the noise (i.e. the variance of the angular signals), the mask values in eq. 1 must be divided by the normalization factor $N_{\rm ph} = \langle \sum_i f_r(r) I_i \rangle$, i.e. the photon flux within the radial weight $f_r(r)$, typically a 0.9 fraction of the full flux. Then, taking advantage of the uncorrelated pixel noise, we sum their contributions to the variance and express the result as

$$S_{\rm noise} = \langle |a|^2_{\rm noise} \rangle = \nu_1/N_{\rm ph} + \nu_2 (R/N_{\rm ph})^2, \quad (6)$$

where the factors ν_1 and ν_2 characterize the contributions of the photon and readout noise, respectively. They depend on the radial mask $f_r(r)$ and on the ring shape, but do not depend on the flux and readout noise:

$$\begin{aligned} \nu_1 &= (1/N_{\rm ph}) \sum_i f_r^2(r_i) I_i, \\ \nu_2 &= \sum_i f_r^2(r_i). \end{aligned} \quad (7)$$

Here the fact that $\langle |a|^2_{\rm noise} \rangle$ is the sum of the cosine and sine variances is used, eliminating the dependence on m: the theoretical noise spectrum is flat. The sense of the noise factors ν is very clear when $f_r(r)$ takes only values of 1 or 0. Then $\nu_1 = 1$ and ν_2 is the number of pixels with non-zero weight, $N_{\rm pix}$. The noise variance is then $(1 + R N_{\rm pix}/N_{\rm ph})/N_{\rm ph}$. The second term in the brackets is the ratio of the readout noise to the average number of photons per pixel. When this ratio is $\ll 1$ (which is the typical situation in practice), the photon noise dominates, otherwise the readout noise is the main contributor to the noise variance of the signals.

The noise variance of the differential sector motion (in pixels) is computed in a similar way by replacing in Eq. 7 quantities $f_r^2(r_i)$ with $f_r^2(r_i)(r_i - r_{\rm ring})^2$. The factor ν_{1r} expresses the variance due to the photon noise and is approximately equal to the square of the ring radial rms width (FWHM divided by 2.35) in pixels. The factor ν_{2r} is larger than ν_2 because the calculation of radius weights pixels in proportion to $(r - r_{\rm ring})^2$ and effectively increases the relative importance of the readout noise. For example, in a simulated data with a sharp radial mask of the width $\Delta r = 1.5\delta r$, the noise factors $\nu_1, \nu_2, \nu_{1r}, \nu_{2r}$ are $1.0, 631, 1.02, 1952$, respectively. The four noise factors are computed during the image cube processing using the average re-centred image to estimate I_i.

Static ring images distorted only by the noise (with optional motion of the ring as a whole over the detector) were simulated and the resulting data cubes were processed by the algorithm described above. Variances of the angular signals and of the differential sector motion were found to match the noise estimates very well, within 10 per cent or better. Furthermore, noise estimates were checked using physical simulation of a static ring image projected on to the camera. The number of photons varied by varying both the illumination and the exposure time. Again, a good agreement between the estimates and the actual measurements was found.

It is instructive to compare the noise variance with the expected scintillation variance. The $m = 1$ WFs in Fig. 3 increases by two orders of magnitude with increasing propagation distance, but the $m = 10$ WF peaks at $\sim 5 \times 10^8\,{\rm m}^{-1/3}$ at small distances and decreases further out. A weak turbulent layer at the ground with $J = 2.1 \times 10^{-13}\,{\rm m}^{1/3}$ ($0.5''$ seeing) would produce an APS of $S_{10} \sim 10^{-4}$. It equals the photon noise for $N_{\rm ph} = 10^4$ which, in our prototype instrument, is a flux from a $V \sim 2$ mag star in a 1-ms exposure. Therefore, subtraction of the noise bias is critical for correct measurement of the weak turbulence near the ground by scintillation, whereas the signal at small m, dominated by the high-altitude turbulence, always largely exceeds the noise. Anyway, the photon noise in RINGSS is much smaller than in MASS, where its calculation and subtraction is even more critical.

4 WEIGHT CALCULATION

Calculation of the theoretical WFs needed to interpret the signal of RINGSS is a vital part of the proposed technique. A WF of any turbulence monitor is computed by the standard method as the integral of the product of the turbulence phase power spectrum $\Phi_\varphi(f)$, the propagation filter $P(f)$, and the instrument frequency filter $Q(\boldsymbol{f})$:

$$W = \int {\rm d}^2 \boldsymbol{f}\ \Phi_\varphi(f) P(f) Q(\boldsymbol{f}), \quad (8)$$

where $\boldsymbol{f}$ is the two-dimensional spatial frequency and f is its modulus. The phase power spectrum is radially symmetric and, for Kolmogorov turbulence, is given by the standard formula (Tatarskii 1961; Roddier 1981)

$$\Phi_\varphi(f) = 0.00969 (2\pi/\lambda)^2 f^{-11/3} J, \quad (9)$$

where the turbulence integral $J = C_n^2 {\rm d}z$ should be set to one in order to compute the WF. The propagation filter for scintillation in monochromatic light,

$$P(f) = \sin^2(\pi \lambda z f^2), \quad (10)$$

is also radially symmetric. Its generalization to polychromatic light is given by Tokovinin (2003). In the case of MASS, the

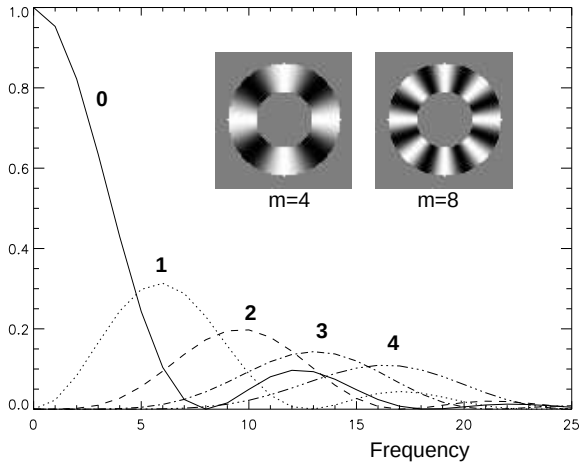

Figure 6. Frequency filters $Q_m(f)$ for the annular aperture with $\epsilon = 0.5$. The inserts show the cosine filters for $m = 4$ and $m = 8$. All filters are normalized to the same integral. The frequency axis is in arbitrary units.

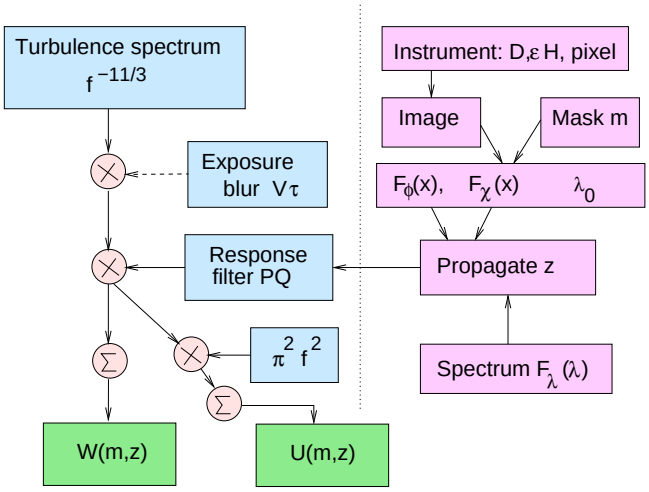

Figure 7. Flow chart of the analytic WF calculation. Blue boxes are 2D arrays in the spatial frequency domain approximating the turbulence spectrum and various frequency filters. The WFs are estimated as integrals (sums) over the frequency. The functions $U(m, z)$ are defined in Section 5.1.

instrument filter is the square modulus of the Fourier transform of the aperture function, normalized to the unit area.[1]

When the scintillation is recorded at the pupil, as in FASS, the function $f_r(r)$ in eq. 1 corresponds to the aperture transmission, and the instrument response filter for the APS S_m has an analytic expression

$$Q_m(f) = \left(2\pi \int_0^\infty f_r(r) J_m(2\pi f r) r \mathrm{d}r\right)^2, \qquad (11)$$

which is the square of the m-th order Hankel transform of the aperture function $f_r(r)$. Figure 6 shows how aperture-plane filters with increasing m isolate different spatial frequency bands. These signals are analogous to the differential scintillation in MASS that also senses a certain frequency band of the scintillation power spectrum, cutting out both low and high spatial frequencies.

The ring images are sensitive to both amplitude and phase fluctuations at the pupil. At large propagation distances, the amplitude fluctuations dominate, and the WFs of RINGSS and aperture-conjugated FASS are very similar, as shown below. However, at small distances the phase fluctuations cannot be neglected. Phase and amplitude fluctuations at the pupil are mutually correlated and are subject to different instrumental frequency filters. It is thus not possible to treat phase and amplitude separately; instead, their joint effect on the signal variance should be evaluated. The propagation and instrument filters are interwined, so the combined response filter PQ in eq. 8 is computed.

One obvious way to tackle the problem is by numerical simulation. However, the WFs estimated in this manner contain statistical noise and their calculation is not fast, especially for polychromatic light where each wavelength must be treated separately; the polychomatic signal a_m is the average of monochromatic signals weighted by the spectral response F_λ.

The analytical formula describing a small-signal response of a general turbulence sensor comes to the rescue. This formula, given in the Appendix of Tokovinin & Kornilov (2007), has been applied in the past to the analysis of DIMM and FADE. Small fluctuations of the signal a derived from the product of the image and mask $M(\boldsymbol{x})$, as in eq. 1, equal

$$\Delta a = \int \mathrm{d}^2\boldsymbol{x}\ F_\varphi(\boldsymbol{x})\ \varphi(\boldsymbol{x})\ + \int \mathrm{d}^2\boldsymbol{x}\ F_\chi(\boldsymbol{x})\ \chi(\boldsymbol{x}), \qquad (12)$$

where $\boldsymbol{x}$ is the spatial coordinate at the pupil plane, $\varphi(\boldsymbol{x})$ and $\chi(\boldsymbol{x})$ are small phase and amplitude wavefront distortions at the pupil, and the functions $F_\varphi(\boldsymbol{x})$ and $F_\chi(\boldsymbol{x})$ represent the instrument response to phase and amplitude, respectively. They equal the imaginary and real parts of the auxiliary quantity $A(\boldsymbol{x})$ given by

$$\begin{aligned} A(\boldsymbol{x}) &= 2\ (\lambda^2 I_0)^{-1}\ E(\boldsymbol{x}) \int \mathrm{d}^2\boldsymbol{x}'\ E^*(\boldsymbol{x}+\boldsymbol{x}')\ \tilde{M}(\boldsymbol{x}'/\lambda) \\ &= 2(\lambda^2 I_0)^{-1}\ E\ [E^* \star \tilde{M}], \end{aligned} \qquad (13)$$

where $E(\boldsymbol{x})$ is the unperturbed complex amplitude of the light waves at the pupil and $\tilde{M}(\boldsymbol{x}'/\lambda)$ is the Fourier transform of the mask. A defocused image corresponds to the quadratic wavefront, $E(\boldsymbol{x}) = \exp(ic|\boldsymbol{x}|^2)$, while for the ring image the wavefront is conic, $E(\boldsymbol{x}) = \exp(ic'|\boldsymbol{x}|)$. Arbitrary aberrations can be accounted for by including them in E.

The formula (13) looks complicated, but its implementation is straightforward. The functions are represented by arrays of 512^2 points (or 1024^2 points in the case of larger apertures). Integrals are replaced by sums, and the convolution between

[1] In a DIMM, the instrument filter is not axially symmetric, while the propagation is often neglected (Kornilov & Safonov 2019).

E^* and $\tilde{M}$ is computed via product of their Fourier transforms. The flow chart of the WF calculation is shown in Fig. 7. For a unit mask, $\tilde{M}(\boldsymbol{x}'/\lambda)$ is the Dirak's δ-function times λ^2, and the response degenerates into EE^*/I_0, i.e. the normalized pupil transmission function. The corresponding signal a is the normalized fluctuation of the total flux, and its variance is S_0. The functions $F_\varphi(\boldsymbol{x})$ and $F_\chi(\boldsymbol{x})$ are computed separately for the cosine and sine masks at a given m, and the corresponding frequency filters are summed in the calculation of PQ.

A turbulent layer at the pupil contains only phase distortions (no scintillation). In this case, the variance of the signal $\langle \Delta a^2 \rangle$ is estimated as the integral of the product of the phase power spectrum Φ_φ and the spectral filter $PQ = |\tilde{F}_\varphi|^2$. However, after propagation, the amplitude and phase fluctuations are modified, and they are, generally speaking, correlated. We cannot apply the phase and amplitude filters separately, but have to 'propagate' them back to the turbulent layer using eq. (A10) from Tokovinin & Kornilov (2007):

$$PQ(\boldsymbol{f}) = |\tilde{F}_\varphi(\boldsymbol{f})\cos(\pi\lambda z|\boldsymbol{f}|^2) - \tilde{F}_\chi(\boldsymbol{f})\sin(\pi\lambda z|\boldsymbol{f}|^2)|^2. \quad (14)$$

This quantity is the frequency filter applied to the phase power spectrum. The integral of their product is the WF for the monochromatic light.

Figure 8 shows how well the monochromatic WFs computed analytically match the results of numerical simulation (crosses) in the case of weak turbulence (small-amplitude scintillation). The same code works for estimation of the WF for a defocused image (suffice to modify the unperturbed amplitude E, replacing the conic wavefront by the spherical one) and for the APS of the pupil-plane scintillation. For a turbulent layer at 4 km, all three WFs are very similar because intensity fluctuations in the ring or in the defocused image resemble the intensity distribution at the aperture. However, the response of an image-plane sensor like RINGSS to a turbulence at 250 m is much stronger because scintillation at the pupil plane after such a short propagation is very small, while phase distortions produce a measurable effect on the ring in the image plane.

The non-monotonous dependence of the WFs on m at small z (see the lower panel of Fig. 8) is related to the fact that the scintillation power spectrum is proportional to $\sin^2(\pi\lambda f^2 z)$, with zeroes at $f_n^2 = n/(\lambda z)$. The signal a_m isolates spatial frequencies around $\pi D(1+\epsilon)/(2m)$ in the pupil plane (see Fig. 6). By setting the propagation distance to $z + H$, we find that the minimum of the WF that corresponds to the first zero of the scintillation spectrum should occur at $m_{\min} \approx \pi D(1+\epsilon)/[2\sqrt{\lambda(z+H)}]$. This crude estimate matches the actual location of the WF minima reasonably well.

In the case of polychromatic light, the scintillation spectrum is damped at spatial frequencies larger than $1/\sqrt{\lambda z}$ (Tokovinin 2003). An analytical expression in that paper was developed for a quasi-Gaussian spectral response $F_\lambda(\lambda)$ proportional to $(\lambda/\lambda_0)\exp[-(\lambda-\lambda_0)^2/2\sigma^2]$ with $\sigma = \Delta\lambda/2.35$. In such case, the cosine and sine terms in (14) are multiplied by the damping factor[2] $\exp[-(1.78/2)(\Delta\lambda)^2 f^4 z^2]$.

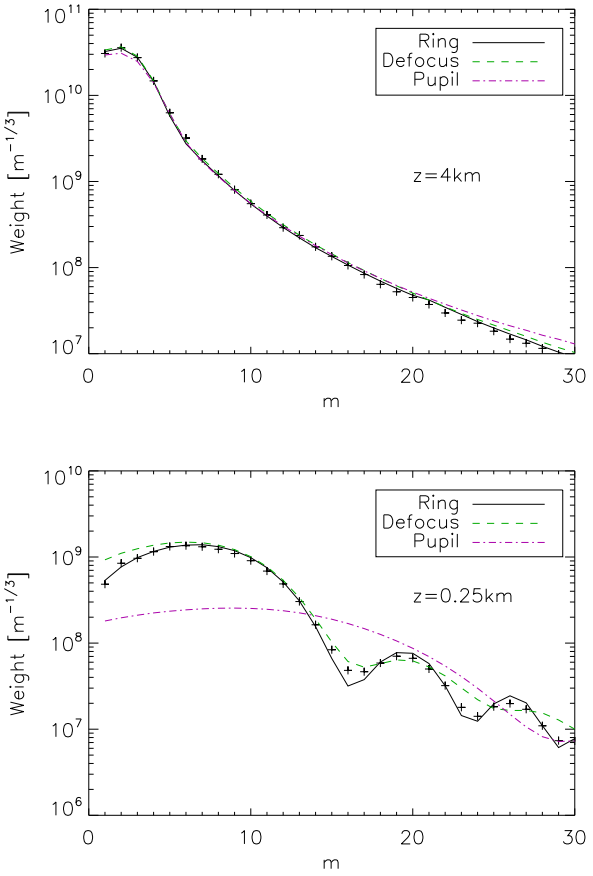

Figure 8. Comparison of the monochromatic WFs of RINGSS computed analytically (solid black line) and by numerical simulation (crosses). The dashed green line is the WF for a defocused image and the dash-dot magenta line is the WF for the pupil-plane scintillation.

For an arbitrary spectral response, the cosine and sine terms in (14) are replaced by the response-weighted sums, e.g.

$$\cos(\pi\lambda z|\boldsymbol{f}|^2) \;\rightarrow\; C\sum_k (F_{\lambda,k}/\lambda_k)\cos(\pi\lambda_k z|\boldsymbol{f}|^2). \quad (15)$$

The normalization constant $C = 1/\sum_k F_{\lambda,k}/\lambda_k$ is chosen to get the unit value of the cosine at zero spatial frequency. This expression is accurate when the spectral response is indeed a set of discrete wavelengths, as in the simulations. When a continuous response is represented by a set of discrete values, the sum in eq. 15 shows 'ringing' at high frequencies. The ringing is suppressed by including the additional damping factor $\exp[-1.5(f^2\delta\lambda z)^2]$, where $\delta\lambda$ is the step of the wavelength grid. The WF calculation for an arbitrary spectral response was

[2] The coefficient is $1.78/2$ because the damping factor is applied here before taking the square modulus of the frequency filter.

checked by supplying a quasi-Gaussian response and comparing the result with the analytical formula.

The functions $F_\varphi(\boldsymbol{x})$ and $F_\chi(\boldsymbol{x})$ (response to phase and amplitude) also depend on the wavelength. This circumstance is neglected here, and they are calculated for the mean wavelength λ_0; only the propagation terms account for the spectral response. Simulations show that this approximation works well.

The WFs plotted in Fig. 3 are calculated for the spectral response of the prototype instrument and a stellar spectrum approximated by a black-body of 7500 K temperature. At angular frequency $m = 10$ and $z = 4$ km, the polychromatic WF is 5.3×10^7 m$^{-1/3}$. The corresponding monochromatic WF in Fig. 8 is 5.0×10^8 m$^{-1/3}$, almost an order of magnitude larger. This example shows that the effect of spectral response is strong and must be accounted for accurately. However, a set of polychromatic WFs for black-body temperatures T from 4000 to 10^4 K can be approximated by linear functions of $\log T$ with an rms accuracy of 5 per cent, sufficient for practical purposes. The influence of the stellar spectrum on the WFs can be reduced by choosing a narrower spectral response of the instrument.

The response coefficient of the differential sector motion in RINGSS is computed by the same algorithm, only the mask functions are different. This coefficient C_r is normalized to express the differential sector motion variance σ^2_{2r} (variance of the sum of radii in opposite sectors in square radians) in one sector in λ/D units for $D/r_0 = 1$,

$$\sigma^2_{2r}(D/\lambda)^2 = C_r(D/r_0)^{5/3}, \tag{16}$$

in analogy with the DIMM response coefficients (Tokovinin 2002). The left hand side of (16) is a dimensionless analogue of the APS, and the right hand side can be viewed as a WF by recalling that $r_0^{-5/3} = 0.423(2\pi/\lambda)^2 J$ and setting $J = 1$. Neglecting for the moment the weak dependence of C_r on the propagation distance, the measured σ^2_{2r} can be converted into the approximate seeing ϵ_0 by the formula

$$\epsilon_0 = 0.98\frac{\lambda}{r_0} \approx 0.98\left(\frac{\sigma^2_{2r}}{4C_r}\right)^{3/5}\left(\frac{D}{\lambda}\right)^{1/5}. \tag{17}$$

In fact, the response of both RINGSS and DIMM depends on the propagation distance z. For the instrument considered here, $C_r = 0.061$ at $z = 0$ and $C_r = 0.043$ at $z = 16$ km. The effect of spectral bandwidth is negligible.

Remember that the WF calculation uses the small-signal approximation where the phase and amplitude fluctuations are much less than one. The validity of this regime is explored in the following Section by means of simulation.

5 MEASUREMENT OF TURBULENCE PARAMETERS

The statistics of the measured coefficients a_m and r_k and the knowledge of the WFs are the two main ingredients needed to estimate the turbulence parameters – seeing, turbulence profile J_j, and the time constant. Bias introduced by the detector noise is estimated using the results of Section 3.3 and subtracted. However, the reduction of variance owing to the finite exposure time and the deviations from the weak-scintillation regime should be corrected in order to get unbiased results.

5.1 Temporal response of RINGSS and the atmospheric time constant

The analysis of temporal effects in this Section closely follows the work by Kornilov (2011). He introduced the quadratic approximation of the APS dependence on the integration (exposure) time τ, valid when the wavefront shift during the exposure, $V\tau$, is less than the scintillation spatial scale (V is the wavefront, or wind, speed). The main expression from the Kornilov's work relates the signal variance $S(\tau)$ for a finite exposure time τ to its zero-exposure variance $S(0)$ by the first-order quadratic formula

$$S_m(\tau) \approx S_m(0) - \frac{\pi\tau^2}{6}\int C_n^2(z)V^2(z)U_m(z)\mathrm{d}z. \tag{18}$$

Here $C_n^2(z)$ is the turbulence strength in m$^{-2/3}$, $V(z)$ is the wind speed, and $U_m(z)$ (U-functions) are analogous to the normal WFs. The U-functions, measured in m$^{-7/3}$, are computed as integrals of the product of the turbulence power spectrum and the square modulus of the spatial filter, but with the additional multiplicative factor of $\pi^2 f^2$ (Fig. 7). The WF calculation code developed here can account for the signal averaging due to a linear blur of $V\tau$ metres and can optionally compute the U-functions together with the normal WFs.

The signal of MASS is sampled continuously. In CMOS cameras, the pixels are read sequentially during each time interval τ by a 'rolling shutter', causing a pixel-dependent shift of the sampling sequence. This minor effect is neglected here. The Kornilov's theory operates with the variances of the signals and their covariances with a time lag of 1, assuming a regular temporal sampling with the cadence τ. Temporal covariances with larger lags are not needed. Let $C_{1,m} = \langle a_{m,i}a^*_{m,i+1}\rangle$ be the covariance of the signal a_m with a lag of one sampling interval and $S_m = \langle|a_m|^2\rangle$ – the variance (assuming zero mean). Then the correlation coefficient $\rho_m = C_{1,m}/S_m$ is the measure of the speed of signal variation. It is close to 1 for slow (well-sampled) signals, but can be small or even negative when the signal varies faster than the sampling time. It follows that the signal variance for double exposure time is $S_m(2\tau) = S_m(\tau)(1 + \rho_m)/2$.

Reduction of the signal variance for double exposure time $\gamma_{12} = S(2\tau)/S(\tau) = (1+\rho)/2$ (the index m is omitted here) is used to estimate the signal variance with zero exposure, i.e. the factor γ_{01}. The analytical WFs show than when the exposure-time reduction is not too severe (i.e. when the blur $V\tau$ is small), the two factors are proportional with a coefficient of 0.4 (Fig. 9). The resulting correction to the zero exposure is

$$S_m(0) \approx S_m(\tau)/(0.8 + 0.2\rho_m). \tag{19}$$

The correction is very good at $\rho > 0.2$ and still acceptable at $\rho > 0$, which implies the maximum exposure-correction factor of 1/0.8=1.25.

The calculation shows that with a 1 ms exposure time, the reduction of the WFs can be substantial, especially at large m. For example, at $z = 1$ km and $V = 10$ m s^{-1}, the correlation

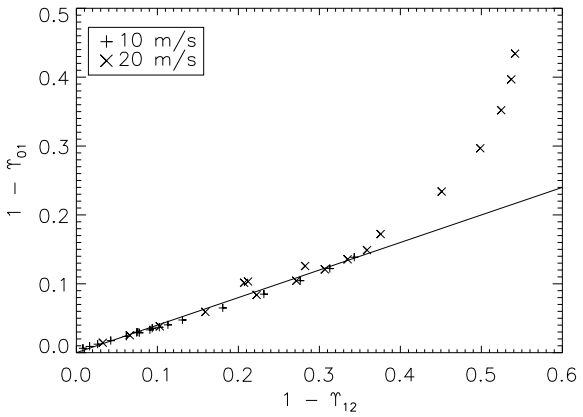

Figure 9. The signal attenuation ratio for the double and single exposure γ_{12} is compared to the signal attenuation for the single and zero exposure γ_{01} for the spatial blurs of 1 cm (plus signs, wind speed 10 m s^{-1} for 1-ms exposure time) and 2 cm (crosses) and various m. The line is $1-\gamma_{01} = 0.4(1-\gamma_{12})$.

coefficient ρ_m drops to zero at $m = 14$ and becomes negative at larger m. At $z = 16$ km and $V = 20$ m s^{-1}, the zero correlation is encountered already at $m = 6$. However, the correlation coefficients ρ_m measured so far experimentally are above 0.6 for all m. Contrary to the simulation, the fastest signals are those with small m. This happens because fast and high atmospheric layers are the main contributors to the small-m signals, while at large m the signal comes mostly from the slow turbulence closer to the ground.

The temporal variation of the RINGSS signals is used to estimate the atmospheric time constant $\tau_0 = 0.31 r_0/\bar{V}$, where $\bar{V}$ is the turbulence-weighted effective wind speed. Although the standard theory uses the mean $V^{5/3}$ as a measure of $\bar{V}$, the second moment of the wind speed V_2 is more relevant for the performance of AO systems and interferometers (Tokovinin et al. 2008):

$$V_2^2 = J^{-1}\int C_n^2(z)V^2(z)\mathrm{d}z, \tag{20}$$

where $J = \int C_n^2(z)\mathrm{d}z$ is the turbulence integral. The corresponding atmospheric AO time constant is $\tau_0 \approx 0.31 r_0/V_2$. The effective wind speed V_2 does not depend on the turbulence strength, r_0, and λ, and is a more meaningful parameter than τ_0.

The difference between (20) and (18) is in the factors U under the integral. The idea of Kornilov is to combine several U-functions with coefficients C_k^U such that

$$\sum_k C_k^U U_k(z) \approx 1, \tag{21}$$

i.e. to remove the dependence on the propagation distance z. Then eq. (18) can be transformed to get

$$V_2^2 \approx \sum_m C_m^U \Delta_m, \tag{22}$$

where the right-hand side contains the measured quantities

$$\Delta_m = 6\frac{S_m(2\tau) - S_m(\tau)}{4\tau^2 - \tau^2} = S_m(\tau)(1-\rho_m)/\tau^2. \tag{23}$$

The coefficients C_m^U are found by solving eq. 21, following the Kornilov's recipe. In other words, we look for a linear combination of the U-functions that is approximately independent of z. The first tests indicated that signals with m of 2 and 4 have very small coefficients C_m^U, while a_6 and a_7 are the strongest contributors. Therefore, the set of U-functions used for the wind estimation in RINGSS is restricted to $m = [1, 3, 6, 7, 8, 9]$. The corresponding coefficients C_m^U are $[9.8, 8.8, 20.2, 19.0, 17.5, 14.6]\times 10^{-15}$ in one representative case. The resulting linear combination of the U-functions deviates from one by less than 0.1 at $z > 1$ km but falls to zero at the ground. Although RINGSS is sensitive to the turbulence near the ground, its estimate of the effective wind speed refers mostly to the free atmosphere, as in MASS. The U-functions and the coefficients C_m^U depend strongly on the spectral response and are re-computed together with the WFs.

5.2 Saturation correction

The theory of all scintillation-based turbulence sensors (SCIDAR, MASS, FASS, RINGSS) is based on the small-signal (weak scintillation) approximation that is not quite fulfilled in the real conditions. The spatial spectrum of a strong (semi-saturated) scintillation differs from the theoretical (weak-scintillation) spectrum by containing more high-frequency power and less low-frequency power. As a result, the APS $S(m)$ increases at large m, imitating a low-altitude turbulence, and the seeing is over-estimated (over-shoots). This effect was extensively studied in the case of MASS, and its partial correction based on numerical simulations was developed by Tokovinin & Kornilov (2007). The idea is to transform the measured APS to the values that would be obtained without saturation and then to apply the standard linear profile restoration algorithm. This strategy is studied here for RINGSS, and it is also applicable to the pupil-plane sensors like FASS.

Figure 10 compares the theoretical (weak-scintillation) weighting functions (WFs) with the results of simulations for monochromatic light to illustrate the impact of the increasingly strong scintillation. For a turbulent layer at 4 km, the classical effect is observed, namely decrease of the power at low frequencies (small m) and its increase at intermediate frequencies, $m > 5$. The cross-over occurs at $m = 4$. Note that at $m \sim 20$ the impact of saturation becomes smaller. For a layer at 1 km, the overall scintillation is smaller, and the effect of saturation is moderate below the cross-over at $m = 8$. However, the WF minimum at $m = 11$ is progressively filled. If the effect of saturation is expressed by the ratio of the simulated and theoretical WFs, there is a strong spike around $m = 11$, reaching a factor of two. Summarizing, there are two distinct effects of saturation: (i) progressive transfer of power to intermediate frequencies at large z and (ii) partial filling of the WF minima at small z. The second effect is specific to RINGSS and is not present when the scintillation is measured at the pupil; it is presumably caused by

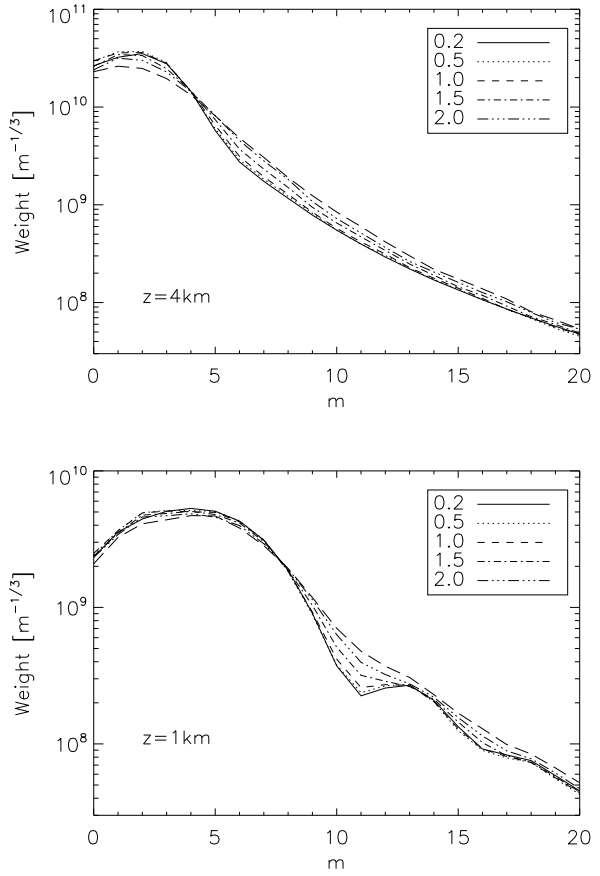

Figure 10. Comparison of the analytic WFs (solid line) with the WFs from numerical simulation for seeing values from $0.2''$ to $2''$ (see the legend box) and a single turbulent layer at 4 km (top) and at 1 km (bottom).

the interplay between the phase and amplitude distortions. This second effect, however, can be neglected in practice because at those frequencies the WFs are an order of magnitude smaller compared to their maximum.

The strength of the scintillation is characterized by the total intensity variance (the Rytov number) s_0^2 (Roddier 1981)

$$s_0^2 = 19.12\lambda^{-7/6}\sum_j J_j z_j^{5/6}. \quad (24)$$

The weak-scintillation regime is valid at $s_0^2 \ll 1$, while $s_0^2 \sim 1$ is the regime of strong (semi-saturated) scintillation. This situation is sometimes encountered in practice. The maximum Rytov variance for the plots in Fig. 10 is 0.80 and 0.25 for $z = 4$ km and $z = 1$ km, respectively. The parameter s_0^2 is not measured directly, but the sum of APS, $S_{\rm tot} = \sum_m S_m$, is a valid substitute because the proportionality $S_{\rm tot}/s_0^2 \approx 0.4$ holds according to the simulations.

A large set of monochromatic simulations was carried out to develop an approximate correction of semi-saturated scintillation, following the MASS prescription (Tokovinin & Kornilov 2007). Each simulation involves two layers with distances ranging from 0.5 km to 16 km, selected randomly from a fixed logarithmic distance grid with a step of $\sqrt{2}$. Turbulence integrals J in these layers are chosen randomly to produce the Rytov variance from 0.05 to 1. The measured APS S_m is compared to the theoretical APS $S_m^{\rm theo}$ calculated from the WFs, i.e. corresponding to the unsaturated regime. Their ratio is approximated by the formula

$$S_m/S_m^{\rm theo} \approx 1 + \sum_{k=1}^{5} Z_{m,k}S_k, \quad (25)$$

where the sum includes a restricted number of terms from $k = 1$ (the $k = 0$ term is not used) to 5. The translation of the measured APS to the quasi-linear one is the inverse of the right-hand part; it approaches one when the scintillation tends to zero.

The set of linear equations (25) is solved by the least squares method to find the coefficients $Z_{m,k}$, called Z-matrix. Two subtleties are relevant. First, only the simulation results with the Rytov variance from 0.05 to 0.7 are used and the cases with the lowest layer at or below 1 km are excluded from the 'training set' used to find Z. Second, the inversion of the system matrix of the least-squares problem is done by the singular value decomposition with rejection of singular values below 10^{-3} of the largest singular value, to avoid the noise amplification. Typically, 3 singular values are rejected.

The matrix correction was determined for all m from 1 to 20 that are used in the profile restoration. Figure 11 gives two representative plots. The quality of the correction is estimated by the rms of the ratio $S_m^{\rm corr}/S_m^{\rm theo}$ computed separately for the training set and for the full set. Overall, the correction works quite well, and the rms residuals for the training set are between 0.05 and 0.09, depending on m. The largest impact of the saturation and, correspondingly, the largest correction, is found for $m = 9$, and the smallest one for $m = 1$ and $m = 2$.

Looking at Fig. 11, one notes that for $m = 8$ the correction works very well not only for the training set, but also for the full set; the rms for the full set is within 0.1. However, for $m = 12$ some blue asterisks are well above one, while the rms for the full set, 0.23, is almost as large as 0.31 without correction. These deviant points correspond to the cases with layers below 1 km, where the minima of the WFs are filled (see Fig. 10, bottom). This phenomenon is not corrected by the current algorithm and for this reason the low-z cases are removed from the training set. The mixture of two different phenomena related to strong scintillation complicated the development of the saturation correction algorithm for RINGSS.

Another, smaller set of monochromatic simulations was made to emulate 1-second image cubes and to test the saturation correction. Without correction, the seeing deduced from the restored turbulence profiles is systematically over-estimated, while the seeing computed from the differential sector motion is underestimated (Fig. 12). The 'overshoots' are caused by the partially saturated scintillation. The energy spilled to a higher spatial frequency is interpreted as coming from a lower but stronger layer, and the seeing is over-estimated. The restored OTP is shifted to

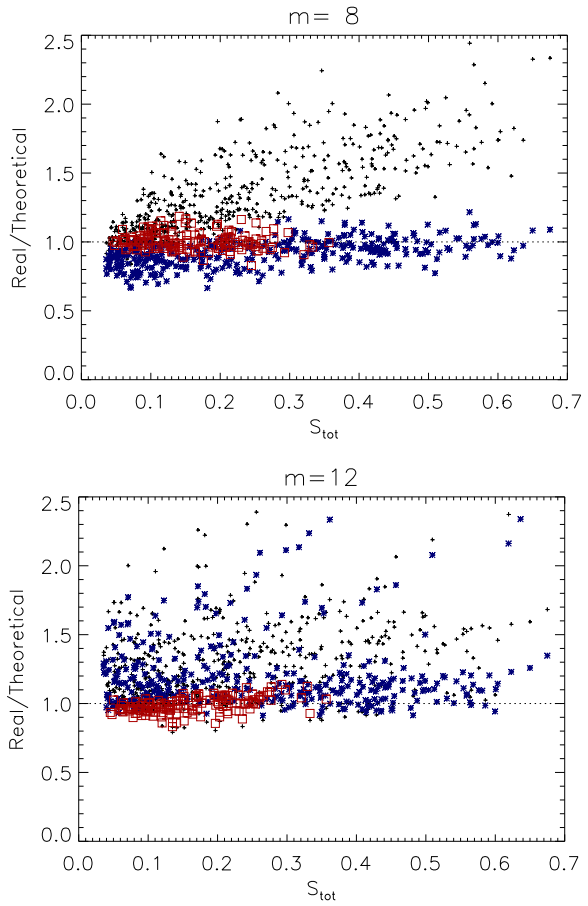

Figure 11. The ratio of the uncorrected to the theoretical power $S_m/S_m^{\rm theo}$ (crosses), the ratio of the corrected power for the training set (red squares), and the same ratio for the remaining cases (blue asterisks) are plotted against $S_{\rm tot}$ for $m = 8$ (top) and for $m = 12$ (bottom).

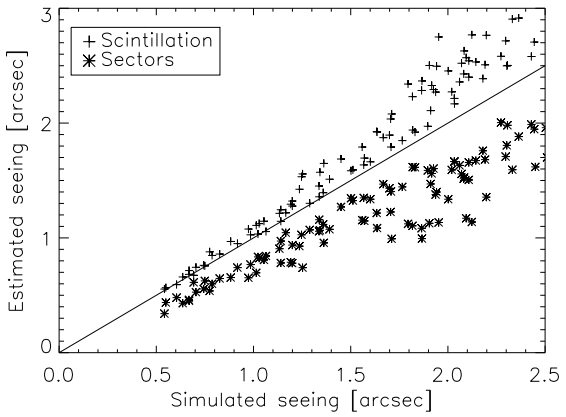

Figure 12. Processing of the simulated image cubes: the seeing deduced from the turbulence profiles restored from the APS (crosses) and estimated from the differential sector motion (asterisks) is plotted against the true simulated seeing, with the straight line corresponding to equality. The saturation is not corrected.

a smaller z, compared to the input OTP. These effects are also observed in MASS.

The seeing deduced from the differential sector motion is under-estimated (under-shoots) for two reasons. First, the decline of the response coefficient $C_r(z)$ at large propagation distances is not taken into account because the distance to turbulence is not known a priori without measuring the OTP. This effect is corrected for by applying the profile-weighted coefficient in eq. 17 to compute the seeing. Secondly, even after this correction, the seeing estimate declines with increasing scintillation approximately as $1 - 0.78S_{\rm tot}$. The division by this empirical factor brings the seeing estimated from the differential sector motion into agreement with the input seeing. Saturation correction also removes the overshoots, and, after the correction, both pluses and asterisks in Fig. 12 align nicely along the diagonal (this trivial plot is not reproduced here).

The Z-matrix correction is a semi-empirical solution to the turbulence profile restoration for a moderately saturated scintillation. This regime is frequently encountered in practice, and the correction seems to be necessary; otherwise, the seeing and free-atmosphere seeing become over-estimated. However, these overshoots remain modest (mostly within 10 per cent) and can be considered as tolerable, especially at good sites. After all, turbulence parameters are always measured with a varying degree of approximation. The latest version of the MASS data reduction software (Kornilov & Kornilov 2011) does not correct for the saturation and is prone to overshoots.

The phenomenon of saturated scintillation is generic, but the correction matrix depends on the instrument parameters. A tool to estimate the Z-matrix from simulations for an arbitrary instrument will be developed by adaptation of the existing code. Qualitatively, the effect of saturation (decrease at small m and overshoots at large m) remains the same for any instrument; it was first noted in MASS.

5.3 Turbulence profile restoration

The turbulence profile is modeled by 9 layers at fixed distances, with 8 layers on a log-spaced grid at 0.125, 0.25, ..., 16 km and the first layer at the ground. This crude model is similar to the one used in MASS, except the additional low layers. Turbulence located between the fixed layers is attributed to the adjacent layers, while its total strength is estimated with a relative error not exceeding 10 per cent. Hence, the crudeness of the distance grid does not contribute substantially to the errors. The z-grid can be optimized in the future.

The OTP, i.e. the 9 values of J_j, is the least-squares solution of eq. 3. To avoid negative J_J, the non-negative least squares method is used, as done by Kornilov & Kornilov (2011) for MASS. The system of equations is over-determined when more than 9 S_m values are used. The estimated noise bias is subtracted from the measured APS. The $m = 0$ term (the full variance) is

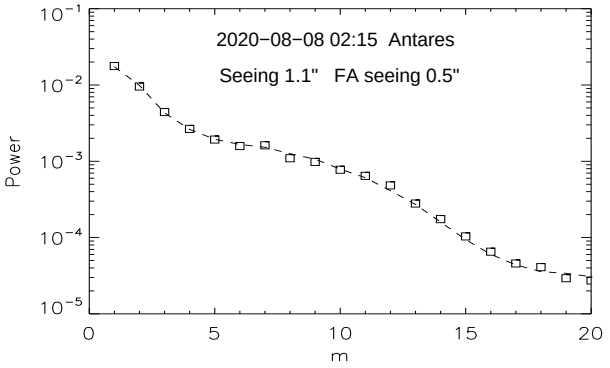

Figure 13. Example of the OTP fitting to the APS computed from a real 2-s data cube. Squares – measured APS, dashed line – fitted model.

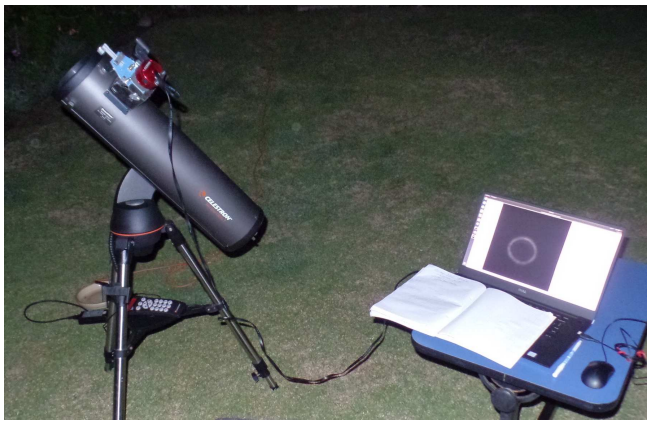

Figure 14. Photo of the RINGSS prototype.

not used because it is not well measured from the short data cubes, being dominated by the slow signal variation, and potentially is affected by variable transparency. The high-order terms with $m > 20$ are also not used because they contain little useful signal. The exposure-time correction (eq. 19) is applied, and the range of m is further restricted to terms with non-negative correlation coefficients ρ_m, but always includes terms up to $m = 9$. This restriction was never necessary for the real data, where all 20 S_m values from $m = 1$ to $m = 20$ are fitted because they have positive ρ_m. Apart from the exposure time, the APS values are corrected for the saturation using the Z-matrix (eq. 25).

Figure 13 gives an example of the OTP restoration using real data. A typical relative rms difference between the measured APS and its model is ∼0.1. Turbulence profiles determined from the successive 2-s records show a similar structure.

The profile restoration is accompanied by the calculation of the effective wind speed V_2 using the pre-computed set of C^U coefficients and applying eq. 22. The wind speed determined from the simulated data matches the input speed, while the real data show a good consistency between successive V_2 estimates.

The total seeing is initially estimated from the differential sector motion by eq. 17 using the coefficient C_r computed for $z = 0$; the 4 estimates of the differential variance σ^2_{2r} from the 8 sectors are averaged and the estimated noise is subtracted. After the OTP is determined, these estimates are corrected for the propagation and for the saturation. The two estimates of the total seeing obtained independently, one from the APS (i.e. from the sum of J_j) and another from the differential sector motion, should agree mutually, providing an overall control of the measurement procedure and biases. Figure 12 illustrates the lack of such agreement when the scintillation is strong and the biases are left uncorrected.

6 PROTOTYPING

This study is devoted mostly to the algorithms and software needed for the turbulence measurement from ring images. However, testing these algorithms on real data is essential to prove that they actually work and to find potential caveats.

A crude prototype RINGSS instrument (Fig. 14) was assembled based on the Celestron Nexstar SLT-130 reflecting Newton telescope with $D = 0.13$ m and central obscuration $\epsilon = 0.45$, defined by a mask behind the secondary mirror (other values of ϵ were also tested). The spiders holding the secondary mirror are so thin that their shadows are not seen in the ring images. The effective focal distance was shortened twice, from the native 0.65 m to 0.35 m, by placing an achromatic doublet lens with a focal distance of $f = 50$ mm at $f/2$ distance in front of the camera. The lens also provides a spherical aberration needed to get sharp rings for a defocus of 1.06 mm that corresponds to the conjugation distance of $H = 400$ m. A yellow filter cuts off the blue light short-ward of ∼450 nm.

The detector is a monochrome CMOS camera ZWO ASI290MM used mostly for amateur astrophotography.[3] The pixel size is 2.9 μm, format 1936×1096 pixels (size 5.6×3.2 mm), readout noise ∼1 el, maximum quantum efficiency (QE) 0.80. The detector is a back-illuminated CMOS chip IMX290 from Sony, uncooled. The high QE and the low noise specified by the vendor were confirmed by our independent characterization of this camera. The conversion factor from ADU to electrons (in the 12-bit mode) is $3.6 \times 10^{-G/200}$, where G is the camera gain setting. With $G = 300$, the conversion factor is 0.11 el/ADU and the readout noise is 1.0 el in most pixels (a 3× larger noise is found in a 0.2 per cent fraction of pixels, which is typical for other scientific CMOS cameras). The spatial uniformity is very good, with a pixel to pixel sensitivity variation of 0.3 per cent rms.

The pixel scale of the prototype is $1.7''$, so the full field of view is about 0.5°; the typical ring radius is 12 pixels or $20''$. Image cubes of 64×64×2000 pixels with 1 ms exposure per frame were acquired using the `ASICap` software from ZWO. A standalone acquisition software for Linux is under development. Figure 15 compares a series of the actual ring images with simulated rings (see also Fig. 5).

Test data were acquired with this prototype at the sea level

[3] https://astronomy-imaging-camera.com/product/asi290mm

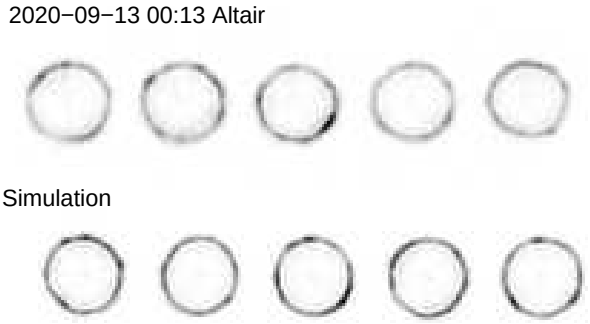

Figure 15. Top: five ring-like 64×64 images recorded with the prototype instrument (ring radius 13.1 pixels, estimated seeing 1.6″). Bottom: five images from a simulated data cube with similar parameters.

Table 1. Main instrument parameters

Parameter	Formula
Ring radius (rad)	$r_{\rm ring,rad} = D(1+\epsilon)/(4H)$
Ring radius (pixels)	$r_{\rm ring} = D(1+\epsilon)F/(4Hp)$
Ring thickness (rad)	$\delta r = 2\lambda/[D(1-\epsilon)]$
Pixel scale (rad)	p/F
Optimum focal ratio	$F/D \approx p(1-\epsilon)/\lambda$
Intrafocal distance (m)	$\Delta = F^2/H$

in La Serena, Chile (access to the Cerro Tololo observatory was closed due to the COVID-19 pandemic). The seeing is poor by the astronomical standards, but some data with a moderate level of scintillation were nevertheless obtained. One example is illustrated in Fig. 16. The data were taken during two short periods separated by 2 hours (the second set begins at the sample 32). The conditions were stable, the estimated wind speed was around 6 m s^{-1}, and the scintillation was small, $S_{\rm tot} \approx 0.1$. During each period, the instrument was pointed to α Aql (V=0.76 mag, spectral type A7V), then to γ Aql (V=2.70 mag, K3II) and back. Crosses in Fig. 16 indicate the star change. The average flux from these stars in 1-ms exposures was 3.1×10^4 and 7.7×10^3 el, respectively. Despite the flux variation by a factor of 4, the change of star does not seem to affect the measured seeing. The WFs were calculated for the effective temperature of 7500 K corresponding to α Aql. The mismatching color of γ Aql does not seem to affect the results strongly. Note that each measurement is obtained from the image cube of only 2 s duration.

7 INSTRUMENT PARAMETERS

In this Section, some considerations on the RINGSS instrument are given. The parameters of the prototype are adequate for turbulence monitoring, but are they chosen optimally?

The main parameters (telescope diameter D, focal length F, central obscuration ϵ, conjugation distance H, and pixel size p) are mutually related. The formulae are given in the text above and repeated in Table 1 for convenience. If the optimum F/D is selected to sample the ring width by 2 pixels, this leads to the formula for the ring radius in pixels that does not depend on the physical pixel size:

$$r_{\rm ring} \approx D^2(1-\epsilon^2)/(4\lambda H). \quad (26)$$

For a fixed 2-pixel ring width, the total number of illuminated pixels is proportional to $r_{\rm ring}$, hence to D^2. The total flux is also proportional to D^2, so the number of photons per pixel remains constant if ϵ and H do not change. However, in order to limit the size of the image cubes, it is advisable to increase H when a larger D is chosen.

A larger aperture collects more photons, produces sharper ring images, and thus substantially reduces the noise of differen-

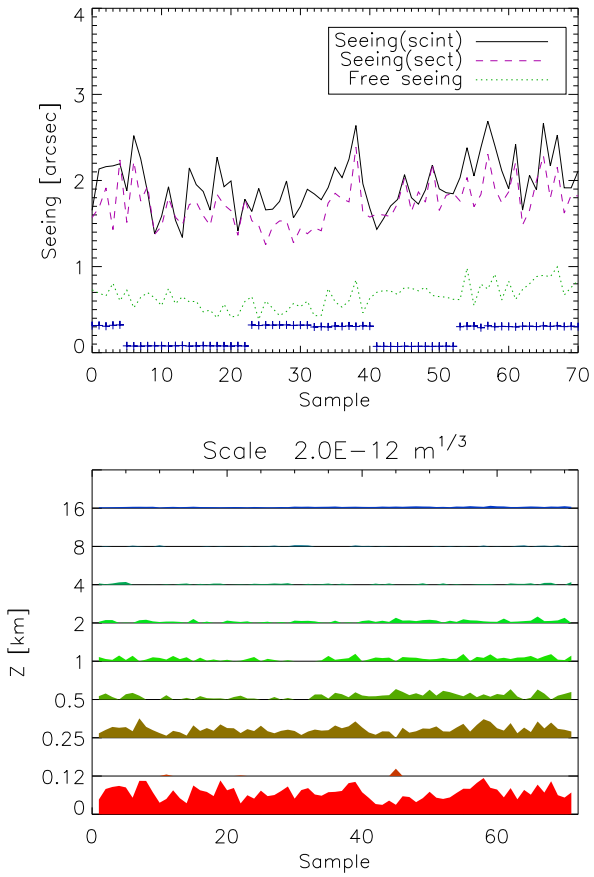

Figure 16. Data from the prototype instrument taken on 2020-09-12. Top panel: the total seeing estimated from the OTP (solid line) and from the differential sector motion (dashed magenta line), as well as the free-atmosphere seeing above 0.5 km (dotted green line), vs. sample number. Blue crosses indicate the flux in arbitrary units to show the change of stars. Bottom panel: OTPs for the same night; the width of each band corresponds to $J = 2\times10^{-12}\,{\rm m}^{1/3}$.

tial image motion measurement. Implementation of the RINGSS concept with $D = 0.2 - 0.3$ m is certainly feasible, although it requires a larger size of the image cubes (see above). The Kolmogorov turbulence spectrum is dominated by the large-scale features; as a result, the amplitude of the wavefront distortions increases as $D^{3/5}$ and the signal to noise ratio in an instrument like RINGSS, DIMM, or FADE also increases with D. However, the use of the full aperture in RINGSS and the modern light detectors with a low noise and a high QE allow us to measure the seeing with smaller apertures (compared to DIMM) with a reasonably low noise. Calculation indicates that with $D = 0.1$ m, the noise of the differential sector motion using a $V = 2.5$ mag star is equivalent to a $0.16''$ seeing, so the noise bias is still moderate and easily accounted for. At $D < 0.1$ m, the noise increases quickly and the seeing measurement by differential sector motion becomes questionable, unless very bright stars are used and the seeing itself is large. The aperture of $D \sim 0.1$ m also matches the Fresnel radius of high-altitude turbulence and is large enough for OTP measurement by scintillation in MASS, FASS, or RINGSS.

Calculations show that the ring thickness is minimum at $\epsilon \approx 0.45$, and such central obscuration is optimal for measuring the differential sector motion. A relatively wide aperture annulus averages the small-scale scintillation, reducing the WFs at large m in comparison with a narrower (larger ϵ) annulus. However, the increase in the photon flux almost compensates for the loss of the scintillation signal, so the central obscuration of $\epsilon \sim 0.5$ is good for measuring both the differential sector motion and the scintillation. In FASS, the scintillation is measured in narrow annular zones chosen inside the aperture (or in the defocused image) to avoid spatial averaging, while in RINGSS the scintillation is averaged in the radial direction.

The choice of the conjugation distance H (or, equivalently, the ring radius) is driven by the compromise. A small H (large ring) gives access to the small-scale scintillation (large m), but its amplitude is also quite small. By increasing H, we get a stronger scintillation from the ground layer and a larger number of photons per pixel in a smaller ring. By setting the minimum ring radius of $r_{\rm ring} = 10$ in (26) and assuming $\epsilon = 0.5$, we get $D = 7.3\sqrt{\lambda H}$, or 7 Fresnel zones across the pupil for the propagation distance H. So, to keep a fixed ring radius of 10 pixels, we need to increase H in proportion to D^2: 0.5 km for $D = 0.13$ m and 2 km for $D = 0.25$ m.

Strong turbulence is typically encountered near the ground. Fluctuations of the ring images caused by the ground-layer turbulence can also be strong, violating the small-signal approximation. This problem is investigated in Fig. 17 by numerical simulation for the case of very poor $2''$ ground-layer seeing. At small H (blue lines), the agreement between the analytical and simulated WFs is quite good, but it becomes worse for the larger H, especially at large m. The minima of the WFs become progressively filled, which is typical for semi-saturated scintillation (compare with Fig. 10). At the same time, the WFs increase with H.

Resuming, the choice of $H \sim 0.5$ km for our prototype appears to be optimal. A smaller H results in the decreased sensitivity to the ground-layer turbulence and in a lower number of

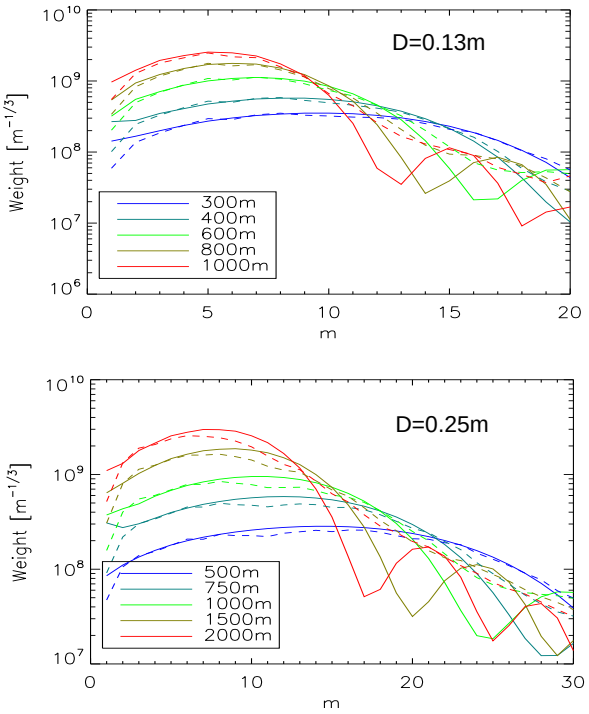

Figure 17. Weighting functions for turbulence at the ground and different conjugation distances H (see the legend box). The full lines are analytical calculations, the dashed lines are derived by simulation assuming a $2''$ seeing and the monochromatic light of $\lambda = 600$ nm. The top plot refers to an aperture of $D = 0.13$ m, the lower plot to $D = 0.25$ m, both for $\epsilon = 0.5$.

photons per pixel, while for a larger H the ring radius would be too small. A larger H should be selected for a larger aperture. A good compromise might be to select $H \propto D$, in which case $r_{\rm ring} \propto D$ also. The exact value of H is not critical as long as it is not very different from the optimum. However, H must be accurately known for correct calculation of the WFs. In practice, the telescope focus should be controlled to keep the ring radius at the desired value.

Keeping a constant defocus (hence a constant ring radius) is also important for getting sharp (diffraction-limited) ring images. As noted above, a conic wavefront is obtained when the spherical aberration and defocus have opposite signs and their rms amplitudes are in a 1:10 proportion. The spherical aberration is defined by the optics, so this optimum ratio corresponds to the specific value of the defocus. Once the H is chosen, the optical design of the system should provide the required amount of the spherical aberration. In the prototype, this is achieved by choosing the focal-reducing lens and the de-magnification factor. Suitable commercial achromatic lenses can be found to provide the desired amount of spherical aberration and focal-distance reduction for almost any feeding telescope, but some residual chromatic aberration might be present as well. A custom lens design would solve this problem. Instead of using a commercial

telescope, RINGSS can be fed by a single concave mirror with suitable focal distance and conic constant, delivering achromatic ring images without any lenses.

The optics of a real instrument is never perfect. The most likely aberrations are astigmatism and coma. I studied biases introduced by the coma and found that a coma up to 2 radian rms is acceptable. The absence of coma is readily controlled by the uniformity of the ring images (see Fig. 5). Careful optical alignment of the feeding telescope and the stability of this alignment are required for RINGSS.

8 DISCUSSION

The new concept of a site monitor emerging emerging from this study is attractive for several reasons. First, its hardware is based on readily available commercial components and is relatively inexpensive, within the reach of an amateur astro-photographer. Second, the telescope aperture needed to monitor the seeing is reduced from the typical 20-30 cm to 10-15 cm. A smaller telescope can use a smaller mount and can be housed in a smaller enclosure; the cost reduction and the increased portability are evident. The relatively large pixels of RINGSS and the short exposure time reduce its sensitivity to the wind shake, compared to a standard DIMM.

While the hardware is simplified, more burden is placed on the software. Its main component is the image-processing tool for measuring the angular intensity variation in the ring images and the fluctuations of their radii. The second key element is the tool to compute the WFs that depend on the instrument parameters and on the spectral response. Once the WFs are known, the estimation of the turbulence profile is trivial, but, as in any seeing monitor, attention should be paid to the correction of biases.

Are the results of RINGSS reliable? This is the fundamental issue for any turbulence monitor. Scintillation sensors are 'self-calibrated' because intensity fluctuations that they record are related to the turbulence parameters by a well-established theory, at least in the weak-scintillation regime. In the case of MASS, departures from this regime must be corrected for, and accurate account of the spectral response is needed; both issues are equally relevant for FASS and RINGSS. Moreover, RINGSS measures the signal close to the image plane, not at the pupil. This makes little difference for a distant turbulence, but a large difference for the near-ground turbulence. However, RINGSS also estimates the seeing by the alternative method of the differential sector motion that is a variant of a DIMM. The agreement between these two independent estimates of the same quantity gives some assurance that both are correct. A similar agreement between MASS and DIMM is observed when turbulence is predominantly high; for RINGSS such agreement should always hold and is a sign of the correct data processing. The results of RINGSS are anchored to the turbulence theory to the same extent as they are for the alternative turbulence monitors, and in this sense they are reliable. Experimental comparison between turbulence monitors, preferably based on different principles, is a useful way to check their biases. However, the idea of 'calibrating' one monitor against another is misleading because none gives totally unbiased results, while the biases depend on many factors, rendering such calibration meaningless. A recent comparison campaign of FASS is reported by Guesalaga et al. (2020).

The number of shortcuts and approximations needed to interpret the signal of RINGSS is impressive. However, similar approximations are involved in any turbulence monitor (although not always recognized explicitly), and the atmospheric theory itself is only approximate. This point is further discussed by Tokovinin & Kornilov (2007) in relation to DIMM and MASS. To give an example, the 'golden standard' of turbulence profiling, SCIDAR, uses analytical monochromatic WFs that neglect pixel and exposure-time averaging (however, see the recent paper by Butterley et al. 2020), while the deviations from the weak-scintillation regime are also ignored (Osborn et al. 2018).

The ability to measure the total seeing, a crude turbulence profile, and the atmospheric time constant is all that is needed for a portable site-testing turbulence monitor. RINGSS is developed with this application in mind. It can also serve as a regular turbulence monitor at the existing observatories, replacing the aging MASS-DIMM instruments.

The RINGSS concept is flexible. It can be applied to both larger and smaller apertures. Existing DIMMs can be converted into RINGSS turbulence profilers by replacing their cameras and software. The concept will also work for defocused images without radial sharpening; however, the number of photons per pixel would be reduced and the alternative seeing measurement by the differential sector motion would be lost. RINGSS with a detector conjugated to the pupil becomes an incarnation of FASS with only a minor difference (the annular aperture is integrated radially in RINGSS but split into narrow rings in FASS).

Historically, the differential image motion was, on one hand, easily related to the seeing theoretically and, on the other hand, technically feasible to measure in the 1980-s and later (at that time, detectors and computers for fast recording of scintillation were either not available or complex). The development of MASS was enabled technically by the progress in electronics and required a matching effort in theory to interpret its data. Nowadays, detectors and computers are cheap and powerful, providing hardware solutions for FASS, FADE, RINGSS, etc. The emphasis is on the theory needed for correct interpretation of their signals and on the associated software.

ACKNOWLEDGMENTS

This work was performed at the NSF's NOIRLab and partially supported by the award 1421197 from the NSF. It is stimulated by the plans to test new astronomical sites. I am grateful to the FASS team (A. Guesalaga and B. Ayancán) for helpful discussions of turbulence profiling, sharing their results, and pertinent comments on this study. Comments by the anonymous Referee are gratefully acknowledged.

DATA AVAILABILITY

No data were generated in this research. The IDL programs used in this work is an experimental software which is not yet ready for public distribution.

REFERENCES

Butterley T., Sarazin M., Le Louarn M., Osborn J., Farley O. J. D. 2020, Proc. SPIE 11448, Adaptive Optics Systems VIII, 114481W doi:10.1117/12.2562559

Guesalaga A., Perera S., Osborn J., et al. 2016, Proc. SPIE, 9909 doi:10.1117/12.2232012

Guesalaga A., Ayancán B., Sarazin M. et al. 2020, MNRAS (2020MNRAS.tmp.3603G) doi:10.1093/mnras/staa3823

Klueckers V. A., Wooder N. J., Nicholls T. W. et al. 1998, A&AS, 130, 141

Kohlman, Christoph *A CMOS based MASS turbulence profiler for the LBT.* Master thesis, Ludwig-Maximilians-University, Munich, 2018

Kornilov V., Tokovinin A., Voziakova O., Zaitsev A., Shatsky N., Potanin S., Sarazin M., 2003, Proc. SPIE, 4839, 837

Kornilov V., Tokovinin A., Shatsky N., Voziakova O., Potanin S., Safonov B., 2007, MNRAS, 383, 1268

Kornilov V. 2011, A&A, 530, 56

Kornilov V. G. & Kornilov M. V. 2011, Exp.Ast, 29, 155

Kornilov V. & Safonov B. 2019, MNRAS, 488, 173

Osborn J., Wilson R. W., Sarazin M. et al. 2018, MNRAS, 478, 8250

Roddier F. 1981, in Wolf E., ed. Progress in Optics, Vol. 19. North-Holland, Amsterdam, p. 281

Sarazin M. & Roddier F., 1990, A&A, 227, 294

Schöck M., Els S., Riddle R. et al. 2009, PASP, 121, 384

Tatarskii V. I., 1961, Wave Propagation in a Turbulent Medium. Dover Press, New York

Tokovinin A., 2002, PASP, 114, 1156

Tokovinin A., 2003, J. Opt. Soc. Am. A, 20, 686

Tokovinin A. & Kornilov V., 2007, MNRAS, 381, 1179

Tokovinin A., Kellerer A., Coude Du Foresto V. 2008, A&A, 477, 671

This paper has been typeset from a TEX/ LATEX file prepared by the author.